













Cite this: *Nanoscale*, 2023, **15**, 8740

# Long-term retention of gold nanoparticles in the liver is not affected by their physicochemical characteristics†

Jennifer Fernandez Alarcon, <sup>‡a</sup> Mahmoud Soliman, <sup>‡b,c</sup> Tanja Ursula Lüdtke,<sup>d</sup> Eva Clemente, <sup>b</sup> Marko Dobricic,<sup>b</sup> Martina B. Violatto, <sup>a</sup> Alessandro Corbelli,<sup>a</sup> Fabio Fiordaliso, <sup>a</sup> Chiara Cordiglieri, <sup>e</sup> Laura Talamini, <sup>a</sup> Giovanni Sitia, <sup>f</sup> Sergio Moya, <sup>d</sup> Paolo Bigini <sup>\*a</sup> and Marco P. Monopoli <sup>\*b</sup>

Gold nanoparticles (GNPs) are considered promising candidates for healthcare applications, however, their toxicity after long-term exposure to the material remains uncertain. Since the liver is the main filter organ for nanomaterials, this work was aimed at evaluating hepatic accumulation, internalisation and overall safety of well-characterised and endotoxin-free GNPs in healthy mice from 15 minutes to 7 weeks after a single administration. Our data demonstrate that GNPs were rapidly segregated into lysosomes of endothelial cells (LSEC) or Kupffer cells regardless of coating or shape but with different kinetics. Despite the long-lasting accumulation in tissues, the safety of GNPs was confirmed by liver enzymatic levels, as they were rapidly eliminated from the blood circulation and accumulated in the liver without inducing hepatic toxicity. Our results demonstrate that GNPs have a safe and biocompatible profile despite their long-term accumulation.

Received 13th February 2023,

Accepted 12th April 2023

DOI: 10.1039/d3nr00685a

rsc.li/nanoscale

## Introduction

The use of nanomaterials for drug delivery and healthcare diagnostics represents a rapidly growing opportunity for precision medicine.<sup>1</sup> Nanoparticle (NP)-conjugated drugs often show a better pharmacokinetic profile than free drugs controlling drug biodistribution and accumulation in specific organs with an improved therapeutic outcome and reduced off-targeting and side effects.<sup>1</sup> To this end, gold nanoparticles (GNPs) have been developed in recent years and their high precision and well-established synthesis methods allow them to be

tuned in size, shape, and a wide range of surface modifications.<sup>2–5</sup> The GNPs surface can also be easily modified with a wide range of small molecules such as nucleic acids, peptides, small interfering RNA, antibodies, polymers such as polyethylene glycol (PEG), and several drugs,<sup>6</sup> making them a very attractive material for nanomedicine. In addition, as an inert metal, gold is not as sensitive to pH variations and is less reactive than silicon dioxide<sup>7,8</sup> or metal-oxide NPs,<sup>9</sup> thus, maintaining their biological characteristics.

Physicochemical properties of NPs, such as the geometry, size, or surface curvature may play a key role in the interactions between NP and cells and tissues, affecting transport and NPs fate. While size plays a fundamental role in retention in filtering organs such as the liver and kidneys, curvature and size affect the rate of internalisation of NPs into cells.<sup>4,5,10</sup> NPs less than 10 nm in diameter have been shown to be energetically unsuitable for uptake into cells<sup>11,12</sup> and, because of their small size, they are excreted through the kidneys *via* urine.<sup>11,12</sup> In contrast, larger NPs with diameters between 10 and 100 nm are preferentially taken up into cells of the liver and excreted from the organism through the hepatobiliary system, with a slower rate of excretion.<sup>11,12</sup> Furthermore, the particle geometry and surface chemistry can drastically alter the fate of GNPs in biological fluids, cells, tissues and organs.<sup>13–16</sup> This modification leads to their uptake in filtering organs, especially in cells of the hepatic reticuloendothelial system (RES), which is

<sup>a</sup>Department of Molecular Biochemistry and Pharmacology, Istituto di Ricerche Farmacologiche Mario Negri IRCCS, Via Mario Negri 2, 20156 Milano, Italy. E-mail: paolo.bigini@marionegri.it

<sup>b</sup>Department of Chemistry, Royal College of Surgeons of Ireland RCSI, St Stephens Green 123, Dublin, Ireland. E-mail: marcomonopoli@rcsi.ie

<sup>c</sup>Physics Department, Faculty of Science, Al-Azhar University, Cairo, Egypt

<sup>d</sup>Department of Soft Matter Nanotechnology, CIC Biomagune, Paseo Miramon 182, 20014 San Sebastian-Donostia, Spain

<sup>e</sup>INGM Imaging Facility, Istituto Nazionale Genetica Molecolare, Via Francesco Sforza 35, 20122 Milano, Italy

<sup>f</sup>Experimental Hepatology Unit, Division of Immunology, Transplantation and Infectious Diseases, IRCCS San Raffaele Scientific Institute, Via Olgettina 58, 20132 Milano, Italy

†Electronic supplementary information (ESI) available. See DOI: <https://doi.org/10.1039/d3nr00685a>

‡Contributed equally as first author.



mainly composed of resident intravascular macrophages (*i.e.*, Kupffer cells)<sup>17</sup> and liver sinusoidal endothelial cells (LSECs), a highly specialised endothelial cell layer with an efficient endocytosis capacity that is among the highest of all cell types in the body.<sup>18</sup> Emerging studies have started to evaluate the NP biological response after chronic exposure,<sup>19,20</sup> but additional studies are required to evaluate the *in vivo* long-term exposure and their translocations in organs.

Herein, we report the biological distribution of GNPs in healthy and immunocompetent mice following a long-term exposition over 47 days and the influence of shape, size, and polymer surface functionalisation on cellular uptake in the liver, subcellular distribution in various liver resident cells, and long-term accumulation in the hepatobiliary system. Our results show that the percentage of GNPs reaching the liver was strongly dependent on size, with small spherical GNPs remaining longer in the bloodstream, whereas up to 70% of nanorods rapidly landed in the liver, the long-term persistence of GNPs in this organ remains unchanged over 47 days after intravenous administration, with GNPs keeping their shape and size even within subcellular compartments of LSECs and Kupffer cells, regardless of geometry and surface functionalisation. Despite the prolonged accumulation in tissues, the overall safety of GNPs was confirmed by the absence of hepatic necroinflammation but should prompt caution in chronic treatments.

## Experimental

### Materials

Before use, all glassware was washed with aqua regia and rinsed thoroughly with Milli-Q water. All chemicals were used as received. Hydrogen tetrachloroaurate(III) hydrate (HAuCl<sub>4</sub>), hexadecyltrimethylammonium chloride (CTAC), hexadecyltrimethylammonium bromide (CTAB), sodium borohydride (NaBH<sub>4</sub>), ascorbic acid (AA), ethyl-3-(3-dimethyl aminopropyl) carbodiimide (EDC), poly(isobutylene-*alt*-maleic-anhydride), hydrochloric acid, 5-bromosalicylic acid, silver nitrate (AgNO<sub>3</sub>), phosphine buffered saline (PBS), ethylenediaminetetraacetic acid (EDTA), resazurin, and dodecylamine (DDA),  $\alpha$ -methoxy- $\omega$ -thiol-poly(ethylene glycol) (MPEG-SH,  $M_w$  = 2 kDa (PEG 2k) and  $M_w$  = 5 kDa (PEG 5k)), poly(sodium 4-styrenesulfonate) (PSS,  $M_w$  = 70 kDa) were purchased from Sigma-Aldrich (UK). Most buffers were prepared manually using Milli-Q water (resistivity of 18.2 M $\Omega$  cm at *ca.* 25 °C).

### Synthesis, functionalisation and NPs characterisation

**Synthesis of spherical GNPs.** Spherical GNPs with core diameters of nominally *ca.* 25 nm and *ca.* 55 nm, named in the following 25-GNPs and 55-GNPs, respectively, were synthesised following the seed-mediated growth method reported by Hanske *et al.*,<sup>21</sup> with some modifications. Synthesis of Au seeds ( $\sim$ 4 nm): freshly prepared NaBH<sub>4</sub> (200 mL, 0.02 M) was injected, under vigorous stirring, into a mixture containing CTAC solution (5 mL, 0.1 M) and HAuCl<sub>4</sub> solution (50 mL, 0.05

M). The solution colour changed immediately to brownish yellow. The seed solution was strongly stirred for 3 min at 1200 rpm and then diluted 10 times in CTAC (100 mM). Seeding growth to 10 nm spheres: a solution of HAuCl<sub>4</sub> (50  $\mu$ L, 0.05 M) was injected, under vigorous stirring, into a mixture containing the seed solution (900  $\mu$ L), AA (40  $\mu$ L, 0.1 M) and CTAC solution (10 mL, 25 mM). After 10 s, the stirring was stopped, and the mixture was left at RT for at least 10 min. The resulting gold nanospheres presented a localised surface plasmon resonance (LSPR) band centred at 521 nm. Growing the 10 nm Au spheres to 25 nm and 55 nm (large scale): briefly, CTAC solution (500 mL, 25 mM) was mixed with AA (2 mL, 0.1 M) and 10 nm spheres (8 mL) to obtain 25 nm GNPs or (1.850 mL) to obtain 55 nm GNPs. Then, HAuCl<sub>4</sub> (2.5 mL, 0.05 M) was injected under vigorous stirring and the mixture was left stirring at RT for at least 1 h. Diluted sodium hypochlorite solution (1 mL, 1 to 1.5 wt% of available chlorine) was injected under a strong stirring and after 5 min of stirring. An additional HAuCl<sub>4</sub> solution (125  $\mu$ L, 0.05 M) was injected in the case of 55-GNPs while no HAuCl<sub>4</sub> solution was added in the case of 25-GNPs. The particle solution was left at 37 °C for at least 2 h to ensure the completion of the oxidation process and achieve NPs with a nearly perfect spherical shape. After that, the GNPs solution was subjected to one-time cleaning by centrifugation (see Table S1† for centrifugation conditions). Then, the supernatant was discarded, and the pellet was dispersed in Milli-Q water and stored for further use.

**Synthesis of gold nanorods (GNRs).** GNRs with dimensions of *ca.* 15  $\times$  55 nm and 15  $\times$  90 nm, named in the following 55-GNRs and 90-GNRs, respectively, were prepared by using the seed-mediated growth method in two steps as reported by Ye *et al.*,<sup>22</sup> (i) preparation of 4 nm Au seeds solution: freshly prepared NaBH<sub>4</sub> (600  $\mu$ L, 0.02 M) was injected, under vigorous stirring, into a mixture containing CTAB solution (5 mL, 0.2 M) and HAuCl<sub>4</sub> (5 mL, 0.5 mM). The resulting brown-yellow colour solution was kept at RT for 15 min before use. (ii) Preparation of growth solution: briefly, CTAB (9.0 g) and 5-bromosalicylic acid (1.1 g) were dissolved in warm Milli-Q water (250 mL). After that, the solution was cooled down to 30 °C, and AgNO<sub>3</sub> (18 mL, 4 mM) for 55-GNRs or (24 mL, 4 mM) in the case of 90-GNRs, were added. The mixture was kept at 30 °C for 15 min and then, HAuCl<sub>4</sub> solution (250 mL, 1 mM) was added. After 15 min of stirring (400 rpm), AA (2 mL, 0.064 M) for 55-GNRs or (1.25 mL, 0.064 mM) in the case of 90-GNRs, were added, and the solution was vigorously stirred for 30 s until it became colourless. Finally, a freshly prepared seed solution (400  $\mu$ L) (as described above) was injected into the growth solution and stirred for 30 s. Finally, the solution was kept overnight at 30 °C without stirring to allow GNRs to grow. The resulting GNRs solution was subjected to one-time cleaning by centrifugation (see Table S1† for centrifugation conditions). Then, the supernatant was discarded, and the pellet was dispersed in Milli-Q water and stored for further use.

**PEGylation of NPs.** PEGylating of NPs was carried out according to the protocol reported by Xu *et al.*<sup>23</sup> Briefly, the



NPs were coated first with PSS, which was exchanged later with PEG 5k. For the PSS coating, a stock solution (0.125 M, in monomer units PSS, one polymer unit ( $C_8H_7NaO_3S$ ) has 206 g  $mol^{-1}$  molecular weight) was prepared in Milli-Q water and stored for further use. A specific amount of PSS solution, calculated using the equations reported in the Appendix† ( $C_p = 0.125$  M, RP/area = 15 000), was added to the NPs solution (100 mL) and the mixture was further stirred for 1–2 min and then left without shaking at RT for 24 h. As a result, PSS molecules were adsorbed to the CTAC/CTAB-coated NPs forming a PSS–CTAC/CTAB complex. After that, the NPs solution was subjected to one-time cleaning by centrifugation (see Table S1† for centrifugation parameters). Thereafter, the supernatant was discarded, and the pellet was dispersed in Milli-Q water. To exchange the PSS–CTAC/CTAB complex, a specific amount of PEG 5k in Milli-Q water (see Table S1†) was added to the solution of PSS-coated NPs and further stirred at RT for 24 h. After that, The PEGylated NPs were subjected to one-time cleaning by centrifugation (see Table S1† for centrifugation parameters), the supernatant was discarded, and the pellet was dispersed in Milli-Q water and stored for further use.

**NPs phase transfer and polymer coating.** For polymer coating, the NPs were transferred from the aqueous medium to the organic solvent following the protocol reported by Soliman *et al.*<sup>3</sup> Briefly, a specific amount of PEG 2k in Milli-Q water (see Table S1†) was added into the NPs solution and further stirred at RT for 24 h. After that, a solution of DDA in chloroform (0.4 M) was added and the mixture was stirred until the NPs were transferred to the chloroform phase. Then, the particles were centrifuged twice (see Table S1†) to remove unbounded organic molecules (DDA and PEG 2k) and the pel was dispersed in chloroform and stored for further use.

The DDA capped NPs were transferred back to Milli-Q water using the polymer coating technique as described by Lin *et al.*<sup>24</sup> The amphiphilic polymer (poly(isobutylene-*alt*-maleic anhydride)) was synthesised by grafting DDA onto its hydrophilic backbone through a spontaneous amide linkage, which converts one maleic anhydride into one corresponding amide and one free carboxylic acid. 75% of the polymer's anhydride rings were grafted by using DDA in THF at 70 °C in order to produce free hydrophobic sides, which will interact later with the hydrophobic sides (hydrophobic chains) of the particles' surface by hydrophobic interaction. The remaining 25% of the anhydride rings will offer the colloidal stability of the particles by electrostatic repulsion of the surface's free carboxylic acids. For details about the synthesis of the amphiphilic polymer used here, we refer to the previous work of Lin *et al.*<sup>24</sup> The resulting dodecyl-grafted-poly(isobutylene-*alt*-maleic anhydride) (in the following referred to as PMA) was dissolved in chloroform as a stock solution (0.5 M). The amount of added PMA per NP was calculated according to eqn (S1)–(S4) in the ESI (Appendix).† The polymer coating was then carried out according to the standard protocol already described.<sup>24</sup>

**Protein corona preparation.** For this purpose, human plasma (HP) and fetal bovine serum (FBS) were allowed to reach RT. Then, NPs (50  $\mu$ g) were injected into either HP or

FBS diluted with PBS solution (10 mM, pH = 7.4) to reach a final concentration of 10% or 80% v/v, respectively. The resulting mixtures were incubated for 1 h at 37 °C and shaken at a speed of 300 rpm. After that, the unreacted unbound biomolecules were washed out using centrifugation as previously described.<sup>4,25</sup> The isolated NP–HC complexes were collected in PBS (20  $\mu$ L) and used for characterisation.

**NPs characterisation.** UV-Vis absorption spectra of the NPs were acquired across a range of wavelengths 400–1000 nm with UV-Vis spectroscopy to study the colloidal stability of NPs after their surface modifications. Measurements were carried out in Milli-Q water with a cuvette path length of  $l_{path} = 1$  cm. The concentration of the NPs was calculated from the absorbance ( $A$ ) at 450 nm (as measured with UV-Vis absorption spectroscopy) instead of using the absorbance at the maximum of LSPR because of the sensitivity of the latter to the deviation in the particle shape, and the refractive index of surface coating and the surrounding medium,<sup>26,27</sup> which can lead to non-preferable results as well described by Haiss<sup>28</sup> and Khlebtsov.<sup>29</sup> For 25-GNPs and 55-GNPs, the molar extinction coefficients of  $\epsilon(450) = 1.10 \times 10^9$   $M^{-1}$   $cm^{-1}$  and  $1.26 \times 10^{10}$   $M^{-1}$   $cm^{-1}$ , respectively, as previously reported by Haiss *et al.*<sup>28</sup> In the case of GNRs samples, the molar extinction coefficient of each sample was calculated from a correlation curve relating NP concentrations determined by ICP-MS with absorption measurements. In this context, ICP-MS measurements were carried out for each sample of GNRs to determine the mass of gold, which was converted later into molar concentration using eqn (S5)–(S7) (Appendix).† Then, the UV-Vis absorption spectra were recorded for a dilution series of each sample, and the absorbance at 450 nm ( $A_{450}$ ) was determined for each corresponding NP concentration of the dilution series. According to formula (S8),† the absorption data were plotted *versus* the NPs concentration, and the curve was fitted with linear regression analysis based on Lambert Beer's law (eqn (S8)†). The respective molar extinction coefficients  $\epsilon(450$  nm) were determined to be  $1.41 \times 10^9$   $M^{-1}$   $cm^{-1}$  and  $2.39 \times 10^9$   $M^{-1}$   $cm^{-1}$  for 55-GNRs and 90-GNRs, respectively. Note that it was assumed that the surface coating does not influence  $\epsilon(450$  nm).

A transmission electron microscope (TEM) was used to characterize the quality of GNPs. The TEM sample was prepared by placing a drop (4  $\mu$ L) of diluted NPs solution on top of a copper grid coated with a layer of carbon and left to dry at RT. The images obtained by TEM were analysed and the core size of at least 100 NPs was manually calculated using the free software ImageJ.

The hydrodynamic diameter ( $d_h$ ) and zeta potential ( $\zeta$ -potential) of a suspension of GNPs (1 mL) were measured by dynamic light scattering (DLS) and laser Doppler anemometry (LDA), respectively. All samples were equilibrated for 5 min at *ca.* 25 °C to ensure NP motion was due to Brownian motion and not due to any thermal gradients. The NPs were measured in Milli-Q water or PBS at 173° backscatter settings, using a 633 nm laser. The determined  $d_h$  [nm] and  $\zeta$ -potentials [mV] were the averages of at least three independent measurements and all data are summarised in Table S2.†



**LAL assay for GNPs.** To evaluate the contamination of the NPs solutions with endotoxin (lipopolysaccharides, LPS) during production or handling, the particle samples were tested using the Pierce LAL Chromogenic Endotoxin Quantitation Kit (88282) purchased from Thermo Fisher. Briefly, an aliquot of the NP stock, equal to an equal amount injected into the mouse, was incubated at 37 °C for 1 h and centrifuged at 11 600g at RT for 30 min. The supernatants were collected and tested for LPS content following the manufacturer's protocol.<sup>30</sup> The detected level of LPS in each NP stock solution was presented in Table S3.†

## Animals and treatments

**Biodistribution in healthy mice CD1.** The Institute for Pharmacological Research Mario Negri IRCCS adheres to the principles set out in the following laws, regulations, and policies governing the care and use of laboratory animals: Italian Governing Law (D.lgs 26/2014; authorisation no. 19/2008-A issued March 6, 2008 by Ministry of Health); Mario Negri Institutional Regulations and Policies providing internal authorisation for people conducting animal experiments (Quality Management System Certificate-UNI EN ISO 9001:2015-Reg. no. 6121); the NIH Guide for the Care and Use of Laboratory Animals and EU directives and guidelines (EEC Council Directive 2010/63/UE). Animal studies were approved by the Mario Negri Institute Animal Care and Use Committee (IACUC) and by the Italian National Institute of Health (code no. 49/2021-PR).

Six-week-old female CD1 mice were purchased from Charles River (Italy) and were maintained under specific pathogen-free conditions (SPF) in the Institute's Animal Care Facilities. Animals were bred in rooms at a constant temperature of  $21 \pm 1$  °C, humidity of  $55 \pm 10\%$  with a 12 h light/dark cycle and *ad libitum* access to food and water. All mice were regularly checked by a veterinarian who is responsible for animal welfare supervision and experimental protocol review. None of the animals died during the study. Mice were randomly divided into eight groups receiving rods and spheres with two different sizes (large and small) and two different polymer coatings (PMA and PEG) ( $n = 5$  for each experimental group). Briefly, all animals received by intravenous injection the same dose of NPs preparation (200  $\mu$ L,  $2 \times 10^{11}$  NPs per mouse). At the selected time points (pre-injection, 15 min, 1 h, 8 h, 24 h, 168 h) mice were anaesthetised and blood was taken from retro-orbital bleeding and serum was analysed for markers of toxicity. Furthermore, at 15 min, 1, 24, 168, 672 and 1128 hours after NPs injection, 5 mice for each group were sacrificed and the organs were collected for histological analysis. Mice perfused were sacrificed by an overdose of ketamine (150 mg  $\text{kg}^{-1}$ ) and metomidine (2 mg  $\text{kg}^{-1}$ ).

**Inductively coupled plasma mass spectrometry (ICP-MS).** Livers and blood were stored at  $-20$  °C until the digestion was carried out. Each sample was thawed overnight before transferring them into a microwave digestion vessel. For the digestion it was used HCl concentrated (1.5 mL, 35%) as well as  $\text{HNO}_3$  concentrated (4.5 mL, 67%) which were added to each vessel

resulting in a ratio of 1 : 3. The digestion vessels were closed and inserted into the speedwave XPERT microwave from Berghof Products + Instruments GmbH. After finishing the digestion, the resulting solution (250  $\mu$ L) was added to diluted aqua regia (2.5 mL, approx. 2%  $\text{HNO}_3$  and 0.5% HCl) and stored until analysis.

The samples were measured by means of the ICP-MS. Before the measurement, ICP-MS set up was calibrated with a freshly prepared serial dilution of gold (Roth, Au-Standard (1000 mg  $\text{mL}^{-1}$ )). The used calibration curve was constructed using gold concentrations from 2 to 2500 parts per billion (ppb). The measurements were carried out with the iCAP-Q ICP-MS (Thermo Scientific, Bremen, Germany) with autosampler ASX-500 (CETAC Technologies, Omaha, USA).

**ALT/AST levels in mice serum.** The extent of hepatocellular injury and toxicity was monitored by measuring serum alanine aminotransferase (sALT). Markers of cell toxicity such as serum aspartate aminotransferase (sAST) activity were measured at 8, 24 and 1128 hours after NPs injection. sALT and sAST activity were measured with a IFCC (International Federation of Clinical Chemistry and Laboratory Medicine) optimised kinetic UV method in an Aries chemical analyzer (Werfen Instrumentation Laboratory S.p.A., Italy) and expressed as  $\text{U L}^{-1}$  (units liter $^{-1}$ ).

Each analysis was validated by a certified biochemical chemist and haematologist specialist using quality control serums (CQI), in the San Raffaele Mouse Clinic.

**Immunohistochemistry.** At the time of autopsy for each mouse, livers were sampled, fixed in 10% neutral buffered formalin (Bio-Optica, Italy) for at least 24 h at RT and then were processed for paraffin embedding. Tissue micrometric sections (4  $\mu$ m in thickness) were cut with Leica RM55 microtome (Leica Microsystem, Italy) and dried into the oven at 37 °C overnight. To visualize the presence of gold agglomerates in the organ parenchyma, autometallography (AMG) staining was carried out, as previously described.<sup>4</sup> Hematoxylin and eosin staining (H&E) was performed in liver sections treated with GNPs and vehicle-treated mice, to provide a general overview of the tissue structure. Hematoxylin stains cell nuclei blue, and eosin stains the extracellular matrix and cytoplasm pink. Nuclei were stained with Mayer's hematoxylin solution (Bio-Optica, Italy) for 2 min and 30 s, and then washed with water until it becomes incolor. The counterstain was carried out in eosin Y solution (Bio-Optica, Italy) for 1 min and 20 s to stain the cytoplasm. Subsequently, slides were washed in tap water until the staining drained out. Samples were dehydrated and mount with xylene-based mounting medium (DPX, Sigma). IBA-1 staining was performed in liver sections treated with GNPs and vehicle-treated mice, to provide a general overview of the macrophage infiltration in tissue. IBA-1 stains macrophages brown and hematoxylin stains the cells' nuclei blue. HIER was performed with citrate buffer pH = 6 for 30 min at 95 °C, endogenous peroxidase inhibition with  $\text{H}_2\text{O}_2$  3% for 10 min at RT, and incubation with blocking solution (PBS-NGS 10%-Tween 20 0.05%) for 30 min at RT. For subcellular localisation, IBA-1 (1 : 200, Wako Chemicals, USA) was used to label





macrophage calcium binding protein, the labelling system ABC kit (Vectastain Elite) and for chromogenic reaction DAB (Sigma-Aldrich). Nuclei were stained with Mayer's hematoxylin solution (Bio-Optica, Italy) for 30 s, and then washed with water until it became colorless. Samples were dehydrated and mounted with xylene-based mounting medium (DPX, Sigma). All images were acquired using Olympus BX61VS.

**Immunofluorescence.** Immunohistochemical analysis in liver was performed in tissue slides of 10  $\mu\text{m}$  cut by cryostat. Tissue sections were fixed in 10% neutral buffered formalin (Bio-Optica, Italy) for 20 min and washed with phosphate-buffered saline (PBS) for 5 min, incubated for 1 h with a blocking solution (PBS-NGS 10%–Triton X-100 0.1%) then washed again with PBS. For subcellular localisation, the following antibodies were used: anti-CD68 (1 : 200, Serotec, Kidlington, UK) was used to label lysosomes and endosome membranes of macrophages, Lyve-1 (1 : 300, Biotechne) was used to label lysosomal endothelial cells and Hoechst-33258 (1  $\mu\text{g mL}^{-1}$  in PBS, Thermo Fisher Scientific) to label nuclei.

**Reflective confocal microscopy.** In order to visualize *ex vivo* the GNPs in mice liver cryo-sections, reflection confocal microscopy was chosen as elsewhere reported for efficient gold reflection.<sup>31</sup> An inverted SP5 true filter-less confocal with 8 laser lines and 4 PMTs was used (Leica Microsystems). The 514 nm laser line was chosen as optimal gold reflecting excitation light, with reflected emission through the opening of AOTF-driven spectral detector in the range of 512–517 nm wavelengths. A 1.40 NA, 63 $\times$  oil objective was used (Leica Microsystems), coupled with system optical zooming-in of 3 $\times$  to 9 $\times$  range, when needed. For gold reflection scanning modality, the confocal pinhole was set at 0.5 A.U. In the sequence of laser-scanning acquisition, besides reflection scan, also transmission signal and fluorescence biological signals were acquired, according to labelled immune-fluorescence reactions. For biological signals scans, the confocal pinhole was set to 1 A.U. Either 1 z-plan acquisition at best focal plan for each field of view, or a 10-micron Z-volume with 0.25-micron Z-step were acquired, according to need. 16-bit depth of signal resolution was acquired over 1024  $\times$  1024 pixel dwell per image with 400 Hz lasers acquisition frequency; laser powers were set on negative control samples as following: 405 nm (10%) for Hoechst signal excitation (nuclear detection) and for transmission, 488 nm (25%) for CD68-(af488) signal, 514 nm (50%) for reflection modality, 633 nm (35%) for Lyve-1-(af647) signal. All PMTs were set on 580–690 V gain range with a  $-1/-2.5\%$  offset range.

For each liver section, a minimum of 15 independent fields of view were acquired to achieve proper quantifications. In order to increase confocal resolution of the reflecting signal, Richardson–Lucy deconvolution algorithm was used, applying the specific module in NIS-Elements software v5.30 (Nikon Instruments/Lim Instruments). Moreover, for quality representation, images were further processed using rolling-ball background suppression and median filtering algorithms (using NIS-Elements v5.30). For image quantifications, raw images without processing were used. Signal thresholding, binarisa-

tion, object classification and segmentation, to detect tissue and cell primary and secondary objects, were performed using an *ad hoc* computed pipeline of analysis within the General Analysis module in NIS-Elements v5.30.

**Transmission electron microscopy (TEM).** At sacrifice, the liver was excised, reduced and fixed with paraformaldehyde (4%) and glutaraldehyde (2%) in phosphate buffer (0.12 M, pH = 7.4) for 4 hours at RT, followed by post-fixation with OsO<sub>4</sub> (1%) in cacodylate buffer (0.12 M) at RT for 1 h. After dehydration in graded series of ethanol, tissue samples were cleared in propylene oxide, embedded in epoxy medium (Epon 812 Fluka) and polymerised at 60  $^{\circ}\text{C}$  for 72 h. From each sample, 1  $\mu\text{m}$ -section was cut with a Leica EM UC6 ultramicrotome (Leica Microsystems), stained with Toluidine blue and mounted on glass slides for light microscopic inspection. Ultra-thin 60 nm-sections of areas of interest were then obtained and counterstained with uranyl acetate and lead citrate, and images were obtained with an Energy Filter Transmission Electron Microscope (EFTEM, ZEISS LIBRA® 120) coupled with an yttrium aluminium garnet (YAG) scintillator slow-scan CCD camera (Sharp eye, TRS).

**Statistics.** All the tests carried out for the physico-chemical characterisation of NPs were performed at least in triplicates. For *in vivo* experiments, the number of animals sacrificed at each data point was minimised ( $n = 5$ ) according to the 3Rs principle. Quantitative data are presented as mean  $\pm$  SEM. The differences between groups were compared using unpaired, two-tailed independent Student's *t*-test or one-way analysis of variance (ANOVA) with repeated measures followed by Bonferroni's *post hoc* analysis used for multiple comparison. No collected data was excluded from analysis. The *p*-value is noted either in the manuscript text or depicted in figures and legends as: \* $P < 0.05$ , \*\* $P < 0.01$ , \*\*\* $P < 0.001$  or \*\*\*\* $P < 0.0001$ . Data was analysed using Prism 5 (GraphPad Software).

## Results and discussion

### GNPs synthesis and characterisation

In this study, we designed a series of GNPs with different sizes, shapes and surface coating in order to define their biological compatibility *in vivo* and define how their physico-chemical characteristics shape hepatic cellular targeting and hepatobiliary clearance. We synthesised four different types of endotoxin-free GNPs, spherical NPs with a diameter of 25 nm (25-GNPs) and 55 nm (55-GNPs) respectively, and rods of 15  $\times$  55 nm (55-GNRs) and 15  $\times$  90 nm (90-GNRs), respectively. Each GNP was functionalised with two different surface coating strategies, either polyethylene glycol (PEG) or poly(isobutylene-*alt*-maleic) anhydride (PMA), both negatively charged, to ensure a higher biosafety profile and high colloidal stability (see Tables S1 and S2†).<sup>3,23,24,32,33</sup> PEG is a well-known anti-fouling polymer which conjugates to the gold surface covalently after CTAB displacement. Meanwhile, PMA can be used as a universal platform for functionalisation. All NPs were synthesised under a laminar flow hood to avoid bacteria



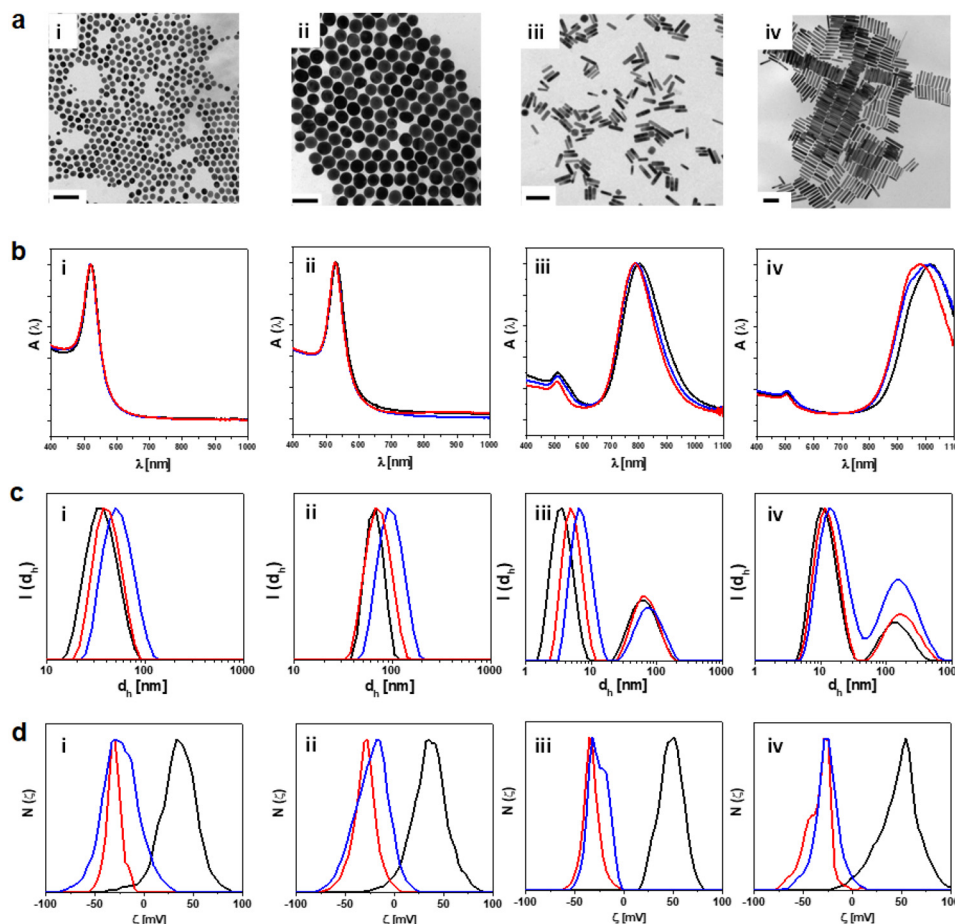


**Fig. 1** Characterisation of GNPs. (a) Representative TEM images of GNPs (with gold core diameters/lengths of (i)  $24.9 \pm 2.66$  nm (25-GNPs), (ii)  $53.97 \pm 4.47$  nm (55-GNPs), (iii)  $56.2 \pm 4.63$  nm (55-GNRs), and (iv)  $91.3 \pm 9.55$  nm (90-GNRs)). Scale bars = 100 nm. Histograms of TEM images were presented in Fig. S2.† (b) Normalised absorption spectra  $A(\lambda)$ . (c) Hydrodynamic diameter  $d_h$  [nm] in intensity ( $d_h/I$ ) and (d)  $\zeta$ -potential distribution  $N(\zeta)$  of (i) 25-GNPs, (ii) 55-GNPs, (iii) 55-GNRs and (iv) 90-GNRs. The colour codes were assigned to the type of surfactant/polymer coated-NPs, hexadecyltrimethylammonium chloride (CTAC)/hexadecyltrimethylammonium bromide (CTAB) (black), PEG-coated NPs (blue) and PMA-coated NPs (red). Triplicates of each measurement included in (c and d) were presented in Fig. S1–S3.†

contamination (*i.e.*, endotoxins), whose presence was tested by using a modified Limulus Amebocyte Lysate (LAL) assay the golden standard assay for detection of LPS (see Methods and Table S3†).<sup>4,25,34</sup>

The characterisation of the NPs is shown in Fig. 1 and Fig. S1–S4.† transmission electron microscopy (TEM) images confirmed a homogeneous size distribution and shape (Fig. 1a). By UV-Vis spectrum a peak absorbance at 524 nm and 532 nm were observed for 25-GNPs and 55-GNPs respectively, meanwhile, rods of 55-GNRs and 90-GNRs have an absorption peak near 510 nm and a second absorption peak of gold nanorods was observed at 820 nm and 1000 nm, respectively (Fig. 1b and Fig. S1†). Following surface coating with PEG and PMA, an increase in size was seen by dynamic light scattering (DLS) (Fig. 1c and Fig. S2, S3†) and a change in the zeta potential ( $\zeta$ ) to an overall negative net charge as a result of new polymer coatings, PEG and PMA (Fig. 1d and Fig. S4†). To evaluate the influence of the NP surface coating on the biomolecular corona formation, we carried out SDS-PAGE in

blood sample media.<sup>15,35</sup> As expected, CTAC/CTAB capped NPs formed a stronger protein corona, particularly 55-GNPs, while the corona formation becomes attenuated for the same NPs coated with PEG or PMA, indicating that both polymers have an antifouling effect<sup>4,35,36</sup> (Fig. S5†).

### Influence of the shape, size and polymer coating on GNPs hepatic biodistribution

RES organs are responsible for removing non-self-bodies from the circulatory system, and it is widely known that in normal physiological conditions, systemically administrated NPs are cleared by this system.<sup>4,11,34</sup> In particular, the mononuclear phagocytic system (MPS) and endothelial cells, such as LSECs, are responsible for pathogen and NP clearance from the circulation, causing their accumulation in the liver, spleen, bone marrow or lymph nodes.<sup>34</sup> However, the long-term fate of specific GNPs with different shapes and surface coating is still unknown. For this purpose, a longitudinal study was carried out to evaluate the short- and long-term fate and biodistribu-



tion of GNPs of different sizes, shapes and surface coatings, where  $2 \times 10^{11}$  NPs were administered intravenously to each mouse, and the samples were analysed at three different time points: 1 hour, 1 and 47 days after injection (Fig. 2). This dose was chosen because it can be compared to other prior studies realised and did not cause toxicity.<sup>4,8</sup> These time points were chosen to exclude the potential toxicity of GNPs after short- and long-term exposure and also study their fate inside the organism. Especially after 1-hour, potential acute toxicity could be detected. After 1 day, nanomaterials' half-life decreases with possible accumulation into tissues. Meanwhile, 47 days is a long time point to evaluate long-term effects, accumulation and possible degradation.<sup>19</sup> In order to monitor the progressive caption, three additional time points were used only with the largest PMA-coated NPs (55-GNPs and 90-GNRs), an earlier time point of 15 minutes, to understand the real contribution of NPs in the circulation and two additional time points after 7 and 28 days to study the progressive accumulation in liver (Fig. 2).

The quantification of the gold content in liver and blood was conducted by inductively coupled plasma mass spectrometry (ICP-MS) analysis (Fig. 3a–f). The data collected was expressed as a percentage of injected dose (% ID), which is calculated from the mass of gold found in the organ divided from the total mass of gold injected in each mouse.

Blood levels of gold showed that, in general, the functionalisation with PEG enhances the overall circulation time in the bloodstream of all GNPs, except for 55-GNPs, in comparison with those PMA-coated (Fig. 3a–d). For PEGylated NPs, 1 hour after treatment, GNRs and 25-GNPs were found with similar percentages around 20 to 30% ID, but after 24 hours almost all GNPs were eliminated from circulation, except for 90-GNRs, with levels around 4% ID. This is in line with the expected

ability of PEG to prevent the adsorption of nonspecific proteins on the NP surface and the formation of the protein corona.<sup>2,37</sup> NPs internalisation inside cells increases with higher adsorption of proteins.<sup>14</sup> 55-GNPs were cleared out from the circulation very rapidly, with less than 1% ID after 1 hour. As previously mentioned, PMA-coated NPs were rapidly cleared out from the circulation in less than 1 hour apart from 25-GNPs (Fig. 3c). Independently from the polymer coating, 25-GNPs were able to remain for a longer time in the bloodstream, with an increase of a 10% ID for PMA-coated NPs in comparison with PEG-coated NPs. This effect has been observed by previous studies, where nanospheres of 10 nm in size had a higher half-time circulation than 50 nm, showing that size can play an important role.<sup>4,38</sup>

Rod-like NPs undergo a faster clearance from blood due to their particular shape, which makes it easier to pass through renal pores and be eliminated through the tubular interspaces with the urine.<sup>39</sup> As shown in Fig. 3b–d, an increase in the hepatic levels of 25-GNPs was observed, with an increase of a 15–20% ID while blood values decrease, demonstrating a clear uptake mostly by the hepatobiliary system. The gold content analysis in the liver of the treated mice showed a progressive accumulation of NPs since early time points. PEG-coated NPs reached the liver after 1 hour of administration with a % ID between 30 to 40 for GNRs and 55-GNPs (Fig. 3b) and maintained the same level regardless of the NP size and shape after 24 hours of the injection. However, long-term exposure resulted in a different NP accumulation, while 55-GNPs value remained constant over time (35% ID), a progressive increase for the other NPs was tested. The highest increase was observed in both GNRs (55% and 70% of ID), this increase could be due to a possible interaction of rods with endothelial cells (EC) in the vessels. The membrane receptors from EC are likely to allow only partial NP phagocytosis due to the high aspect ratio, and could cause a progressive release back into circulation followed by liver filtration.<sup>12</sup> The pharmacokinetic analysis of PMA-coated NPs was found to be influenced by their size, 25-GNPs had a lower penetration inside the liver in comparison with the other GNPs, with just a 10% ID (Fig. 3d). Different studies have observed that large NPs, around 50 nm, were internalised inside cells requiring receptor-mediated endocytosis, through a re-arrangement of the cell cytoskeleton.<sup>12</sup> For this reason, 55-GNPs were able to penetrate inside the liver with around 50% ID. Meanwhile, smaller NPs uptake is less efficient, as the process is more energy demanding due to the membrane re-arrangement for the uptake.<sup>40</sup> Also, a strong increase of uptake was found in rod-like NPs, with a 60 to 75% ID only after the 1<sup>st</sup> hour of administration and the levels remain similar over time. When PMA-coated GNPs interact with the liver, they are strongly retained inside.

To understand in higher detail the pharmacokinetics of PMA-coated NPs inside the liver, 55-GNPs and 90-GNRs, were injected into mice and sacrificed 15 minutes after the treatment. As shown in Fig. 3e, ~20% of ID was found in the liver for 55-GNPs and 30% ID for 90-GNRs, with a significant difference between 15 minutes and 1 hour treated mice showing a

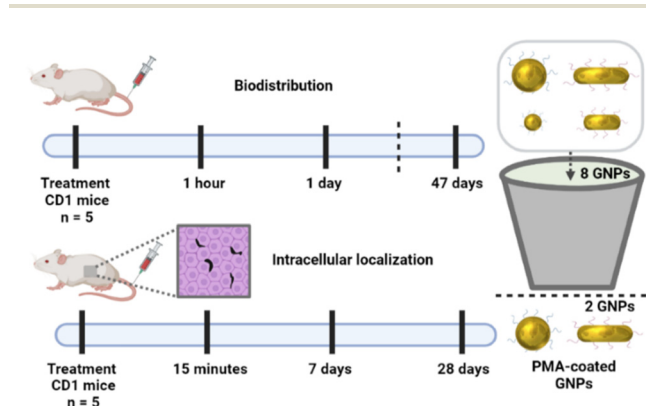


**Fig. 2** Experimental scheme and quantification of gold content in liver and blood by ICP-MS. CD1 mice, six-week-old female were randomly distributed ( $n = 5$ ) and treated *via* intravenous with  $2 \times 10^{11}$  NPs per mice of GNPs suspended in water or left non-treated. Animals were treated with 8 different GNPs in a single dose and sacrificed at three different time points (1 hour, 1 and 47 days) to study the hepatic biodistribution and kinetics. The largest PMA-coated NPs (55-GNPs and 90-GNRs) were selected to evaluate three additional time points (15 minutes, 7 and 28 days) for intracellular sub-localisation and biodegradation.



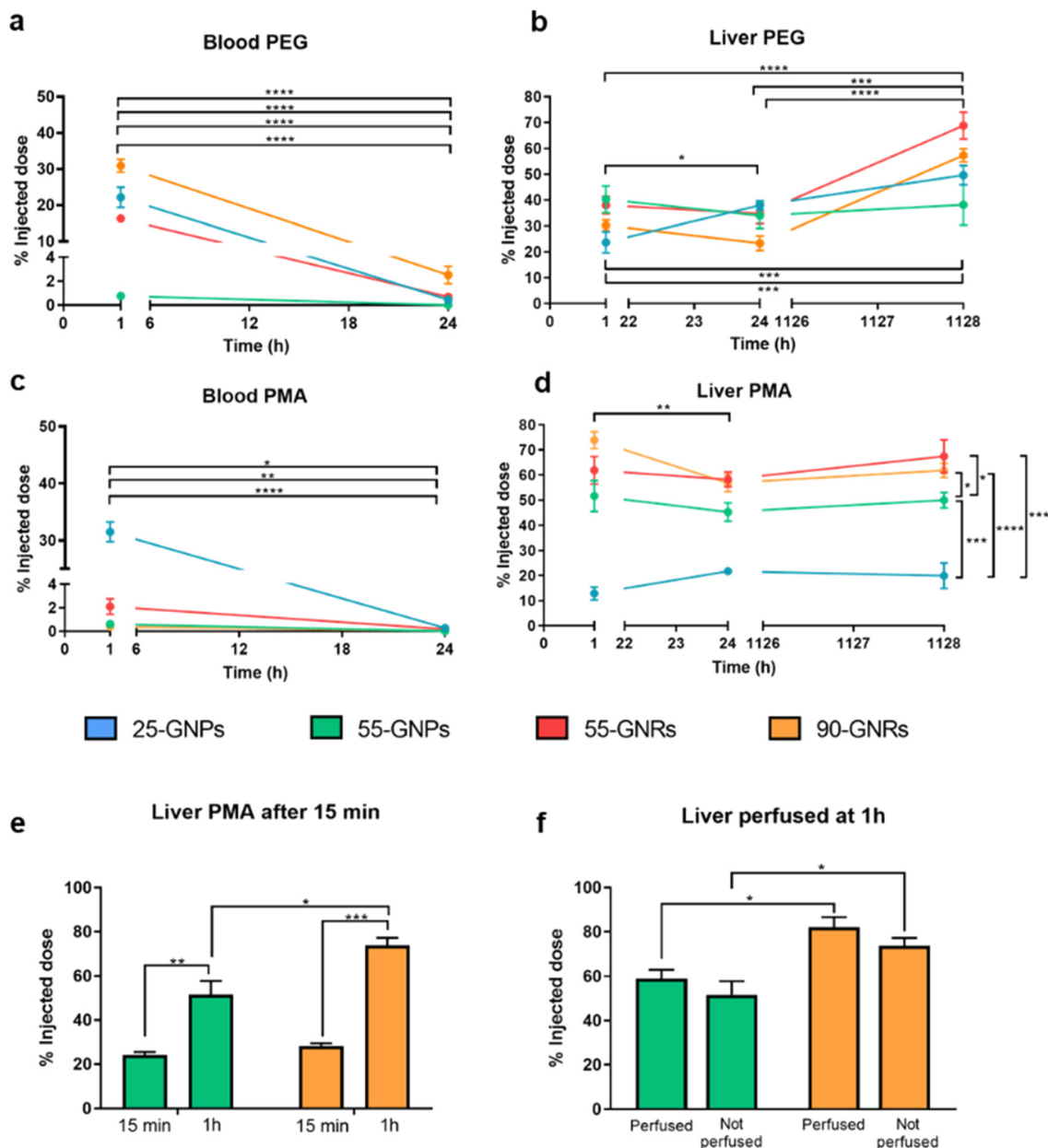


**Fig. 3** (a–d) Percentage of injected dose (% ID) measured by ICP-MS in blood (a–c) and in liver (b–d) derived from mice treated with 8 different GNPs at 1, 24 and 1128 (47 days) hours after treatment. (e) Percentage of injected dose (% ID) in liver from mice treated with PMA-coated GNPs (55-GNPs and 90-GNRs) after 15 minutes and 1 hour. (f) Percentage of injected dose (% ID) in liver from mice treated with PMA-coated GNPs (55-GNPs and 90-GNRs) at the same time point, 1 hour, comparing a perfused liver with a not perfused. Data were presented as mean  $\pm$  S.E.M. of  $n = 5$  mice.  $P$  values were determined by one-way ANOVA with Bonferroni's correction and unpaired Student's  $t$  test (two tailed) \* $P < 0.05$ , \*\* $P < 0.01$ , \*\*\* $P < 0.001$  and \*\*\*\* $P < 0.0001$ .

clear trend in PMA kinetics. As gold detection by ICP-MS does not allow to distinguish between NPs translocated into the tissues and the ones still in circulation in the blood vessels, we compared the gold content of perfused (where the blood was removed by intracardial perfusion) and not perfused livers. Interestingly, no difference in gold content was observed indicating that after 1 hour, GNPs are firmly translocated into the liver tissue rather than being transient into the circulatory system of the organ (Fig. 3f and Fig. S6†).

Overall, ICP-MS analysis had shown that NP polymer coating type had an influence on the GNPs retention in the liver, where PMA-coated GNPs rapidly accumulate inside the liver while PEG-coating increase the circulation in blood. However, other NPs properties, such as the shape, played an important role, where rod-like NPs had a higher retention into the liver than spherical ones. Regardless of the liver kinetic differences, it is important to underline that, independently of the GNPs properties, gold accumulated in liver remained 7





weeks after injection, suggesting that the accumulation is not followed by a clearance over time. *In vivo* similar results were found in mice after 15 months of a single administration without showing any toxic effect.<sup>41</sup> However, *in vitro* studies suggested the formation of extracellular reactive oxygen species (ROS) which helped to degrade elemental gold to ionic gold *via* a Fenton reaction.<sup>19</sup>

### Influence of the shape, size and polymer coating on the cellular uptake

While ICP-MS provided information on the gold content per organ and the fate of the GNPs, it does not bring information

on the cellular mechanisms implicated in the GNPs uptake nor the impact of the chemical modifications on the ' fate administrated intravenously. To this aim, qualitative histological studies revealed a marked increase of GNPs inside hepatic cells by autometallography silver staining (AMG) (Fig. 4) and we focused the analysis on PMA-coated NPs of 55-GNPs and 90-GNRs due to their differences in the liver accumulation kinetics.

Polarised and elongated black spots were already visible in the liver of mice sacrificed 15 minutes after the treatment (red arrows) due to an interaction of GNPs with liver sinusoidal endothelial cells (LSECs) (Fig. 4a, b and Fig. S7, S8†).

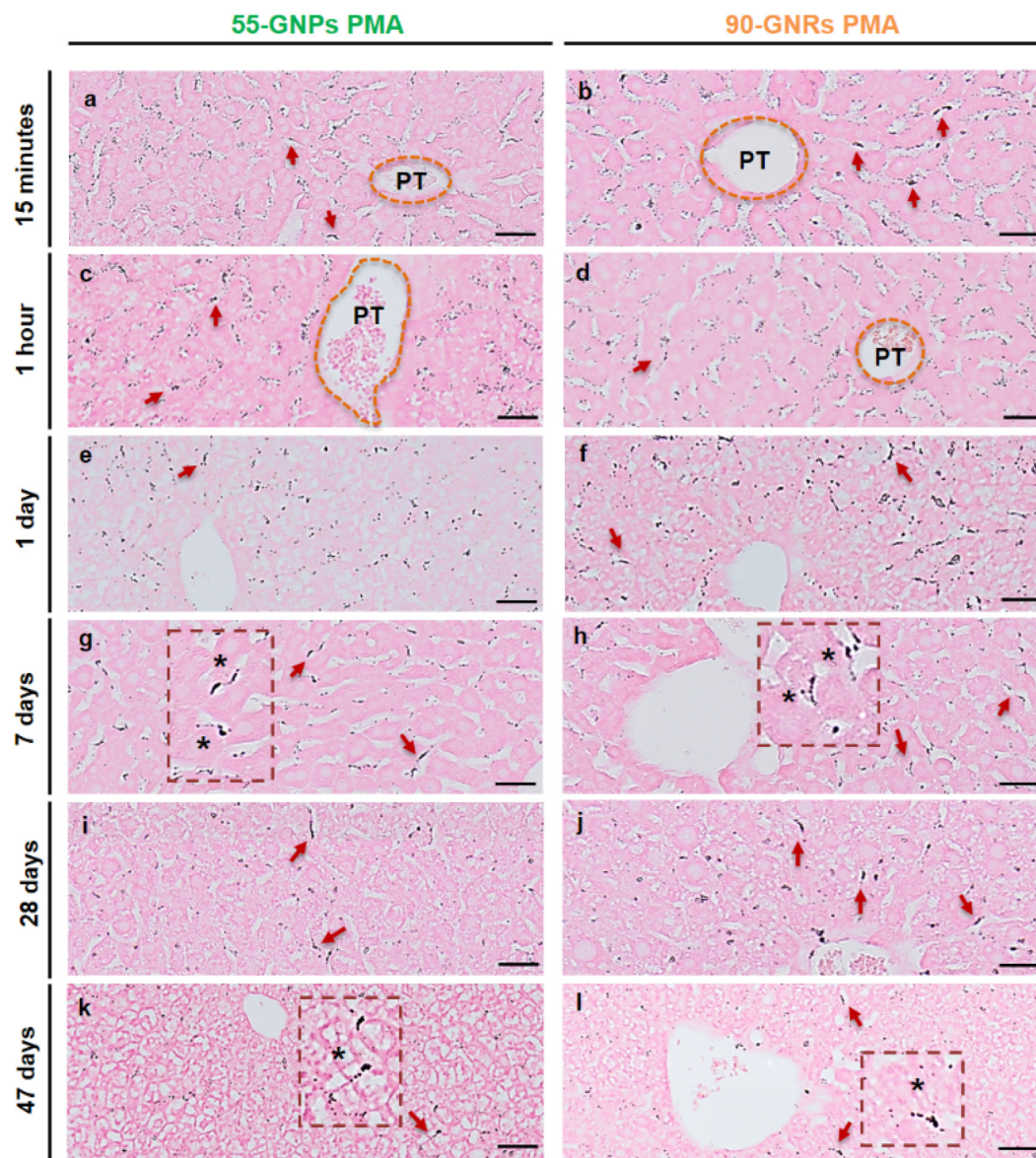


**Fig. 4** Histological evaluation of gold distribution (black spots) in liver tissue by AMG. Representative micrographs of liver from mice treated with PMA-coated NPs, 55-GNPs (left column) 90-GNRs (right column) and sacrificed after (a and b) 15 minutes, (c and d) 1 hour, (e and f) 24 hours, (g and h) 7 days, (i and j) 28 days and (k and l) 47 days after GNPs administration. Red arrows showed silver-stained GNPs inside hepatic cells. Orange dotted lines showed GNPs circulating from the portal triad (PT). Black asterisks showed silver-stained GNPs magnifications inside hepatic cells. Scale bars for AMG images = 20  $\mu$ m (large image) and 20  $\mu$ m (small insets).



As expected, surrounding areas near the central vein had a lower signal as NPs were circulating from the portal triad (dotted lines in Fig. 4a–d and Fig. S7†) causing NPs penetration inside the sinusoids (Fig. S7†). After 24 hours, it was observed a visible rise in the black spots localised inside elongated bodies due to a possible uptake of GNPs by Kupffer cells (liver macrophages) or LSEC (Fig. 4e and f), with a simultaneous decrease in the NPs levels found in the sinusoids. Over time, NPs signal slowly and progressively decreased in liver parenchyma (Fig. 4g–j), and after 47 days it was possible to detect GNPs internalised inside hepatic cells (Fig. 4k and l). No differences were observed in terms of signal intensity or parenchyma biodistribution between both NPs, the behaviour inside the liver was very similar.

The evaluation of GNPs biodistribution by AMG is extremely important to have a topography of NP accumulation in the liver. To obtain more information regarding their cellular fate, intracellular localisation and stability, we carried out TEM as gold is an optimal material for this type of analysis due to its electron-dense metallic core that provides enough contrast with the surrounding biological environment, being easily identified in tissues. TEM analysis has shown that GNPs could be easily detected in the tissue section already after 15 minutes of injection, with the GNPs shape and morphology well preserved regardless of the NP type and time point of analysis (Fig. 5). Representative TEM images of GNPs were exclusively observed in Kupffer cells and LSECs with no sign of NPs in the hepatocytes or liver parenchyma where the GNPs are

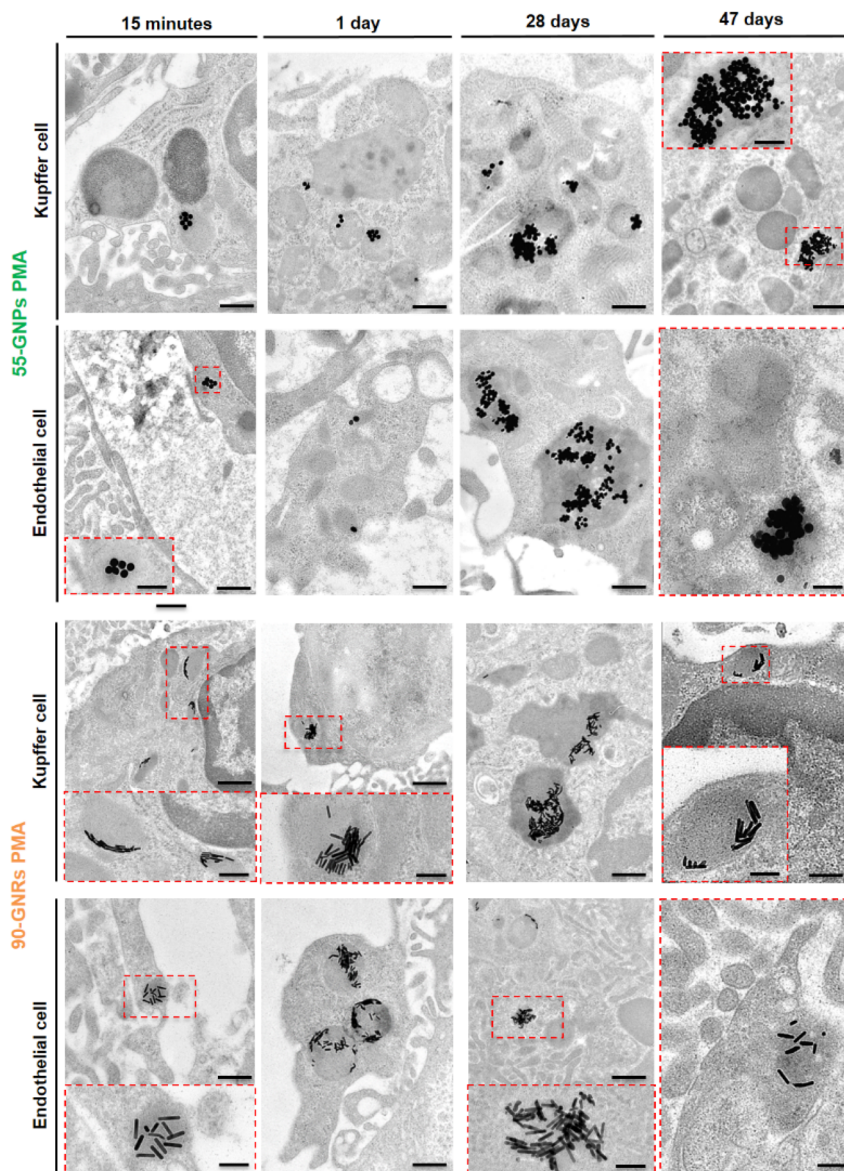


**Fig. 5** Ultrastructural localisation of GNPs inside liver cells by TEM. Representative TEM images of PMA coated NPs 55-GNPs and 90-GNRs in healthy mice treated at four different time points (15 min, 1, 28 and 47 days). Images showed GNPs internalised in lysosomes (small insets) of Kupffer cells and LSEC. No GNPs were observed after 47 days. Scale bars for TEM images = 1  $\mu$ m (large image) and 200 nm (small insets).





rapidly translocated into the cells and accumulate in secondary lysosomes. This is a common terminal step of endocytosis and phagocytosis, formed by the fusion of a primary lysosome with phagosomes or endosomes, and consequent activation of digesting enzymes like acid hydrolases, which are an indicator of a pH change from  $<6^{42}$  to 4.5.<sup>43,44</sup> The number of GNPs agglomerated in the cluster after 1 and 28 days was observed to increase over time (Fig. 5) and despite the strong presence of this cluster, the internalisation did not affect the ultrastructural organisation of both Kupffer cells and LSECs showing

perfectly preserved organelles such as endoplasmic reticulum, Golgi apparatus, nucleus and a great quantity of primary lysosomes. Interestingly, after 47 days from the single injection, it was still possible to detect GNPs inside Kupffer cells and LSECs (Fig. 5), confirming that GNPs lysosomal degradation into ionic gold and the following reassembling into nanoleaves already observed *in vitro* after 2 weeks was exclusively taking place for smaller GNPs (up to 22 nm).<sup>19,31</sup> This study was important to understand in which cells and organelles GNPs were internalised and if they remain or migrate over time.

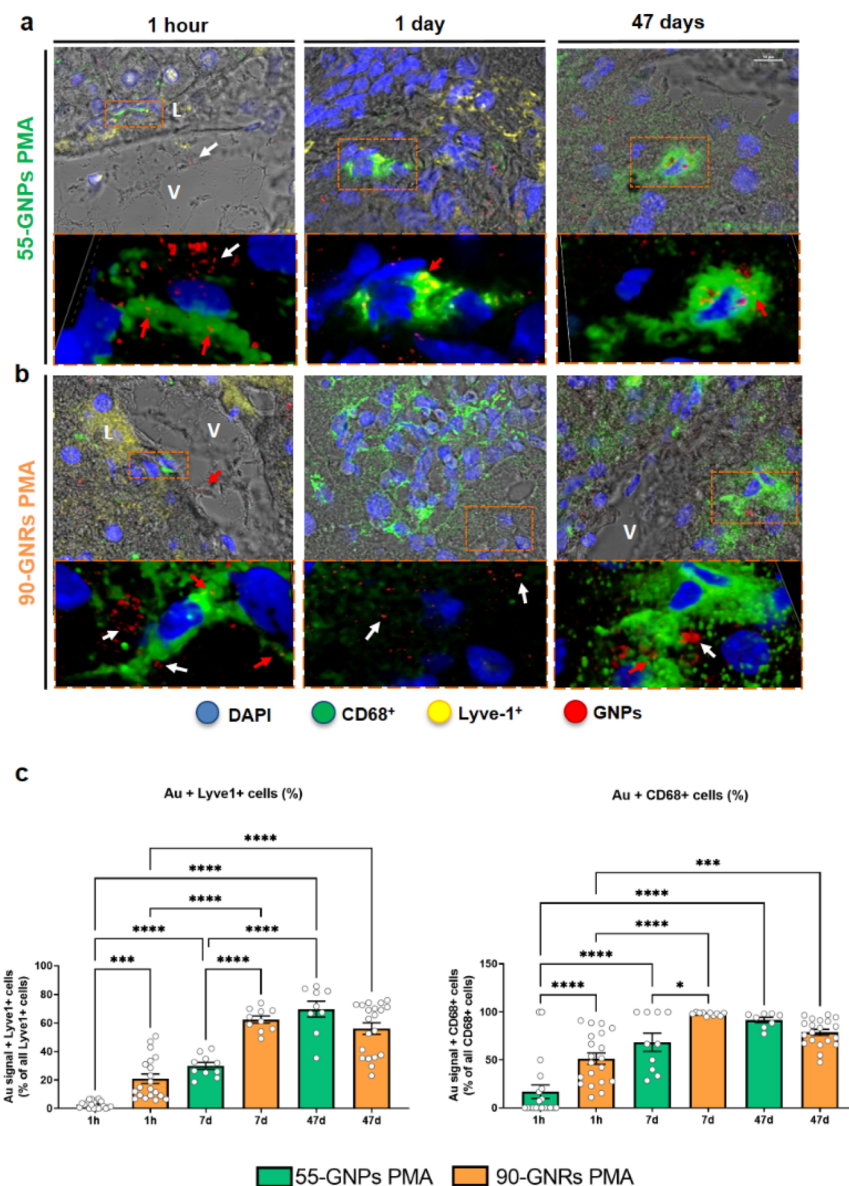


**Fig. 6** Co-localisation of GNPs in hepatic tissue. (a and b) Reflective SIM in liver sections from healthy mice treated with PMA-coated NPs (a) 55-GNPs and (b) 90-GNRs at three different time points (1 hour, 1 and 47 days). In blue, it was shown the nuclei (Hoechst), in green the macrophages (CD68), liver sinusoidal endothelial cells were depicted in yellow (Lyve-1) and in red GNPs (Au-reflective signal). White arrowheads showed reflected Au signals in inter-cellular proximity to macrophages (CD68+ cells) and by red arrowheads the intra-cellular localisation. (V) Indicated enriched vessel with Au-signal and (L) the edge of Lyve-1+ cells. (c) Quantification of the area occupied by GNPs in CD68+ and Lyve-1+ cells in liver sections from treated healthy mice at three different time points (1 hour, 7 and 47 days). Data were presented as mean  $\pm$  S.E.M. P values were determined by one-way ANOVA with Bonferroni's correction \* $P < 0.05$ , \*\*\* $P < 0.001$  and \*\*\*\* $P < 0.0001$ . Scale bars = 10  $\mu$ m (large images), 2.5  $\mu$ m (small insets).



To obtain quantitative data related to the segregation of the NPs inside Kupffer cells and LSECs, a co-localisation study was performed by using structured illumination microscopy (SIM) where the NP presence was detected by measuring the reflected light on the GNP surface.<sup>31</sup> Macrophages and ECs were immunostained using fluorescent antibodies against CD68 and Lyve-1, respectively (Fig. 6 and Fig. S9, S10†).

We observed clusters of GNPs reflective signals after 1 hour of treatment (Fig. 6a) where most of the NPs aggregates were found in the peripheral areas of CD68<sup>+</sup> cells and parenchymal proximities to the sinusoids, due to a fast interaction between GNPs with LSECs, while only small aggregations of NPs were still visible in the vessels after 1 hour from injection. Aggregates of 55-GNPs reflective structures were already visible intracellularly within CD68<sup>+</sup> cells at 24 hours from the injection, where GNPs were retained in the lysosomes, forming little vesicles of clustered laser-reflecting structures as shown in Fig. 6a. Meanwhile, 90-GNRs reflecting structures were visible both in the intercellular spaces surrounding CD68<sup>+</sup> cells (white arrowheads) and within intracellular areas (red arrowheads) (Fig. 6b). A similar behaviour was exhibited after 47 days where GNPs were still visible inside the hepatic cells (Fig. 6a and b).

Whereas the total percentage of Lyve-1 and CD68 cells reflection from internalised GNPs was approximately similar (Fig. 6c and Fig. S11†), a relevant difference was observed between sphere-shaped and rod-shaped GNPs. Inside Kupffer cells, 55-GNPs rapidly formed small clusters evidencing an easy passage inside the cell through endocytosis. In contrast, rod-like NPs formed smaller clusters in the surrounding areas of the phagocytic cells, due to a lower internalisation rate despite the fact that they had a faster interaction with hepatic cells. If nanorods are not orientated in the correct direction towards the cell membrane,<sup>45</sup> as they are more elongated due to a larger length-to-radius, phagocytosis is slower.<sup>21,46</sup> Despite the multivalent cell membrane receptors, rod NPs may be too large, and their uptake may not be possible due to a partial wrapping and resulting in the particle releasement back into the hepatic system, followed by the uptake by another phagocytic cell in the proximity.<sup>2</sup>

Regardless of the detection and imaging methodologies used, our data strongly suggests that, although the physico-chemical properties play a role in the total amount of NPs filtered by the liver, they do not seem crucial in terms of: (1) kinetics (very fast in the first hours after administration); (2) cellular segregation (they exclusively penetrated in LSECs and macrophages) and; (3) longer lasting aggregation.

### Liver nanosafety

Ultrastructural analyses by TEM did not reveal marked cellular alterations in animals treated with GNPs. However, since the liver plays a major role in metabolic processes of so many drugs, to ensure that no toxic effect was caused by the NPs inside the hepatic system, a toxicological study was performed with liver tissue and serum (Fig. 7 and Fig. S12, S13†). The serological levels of alanine transaminase (sALT) and aspartate

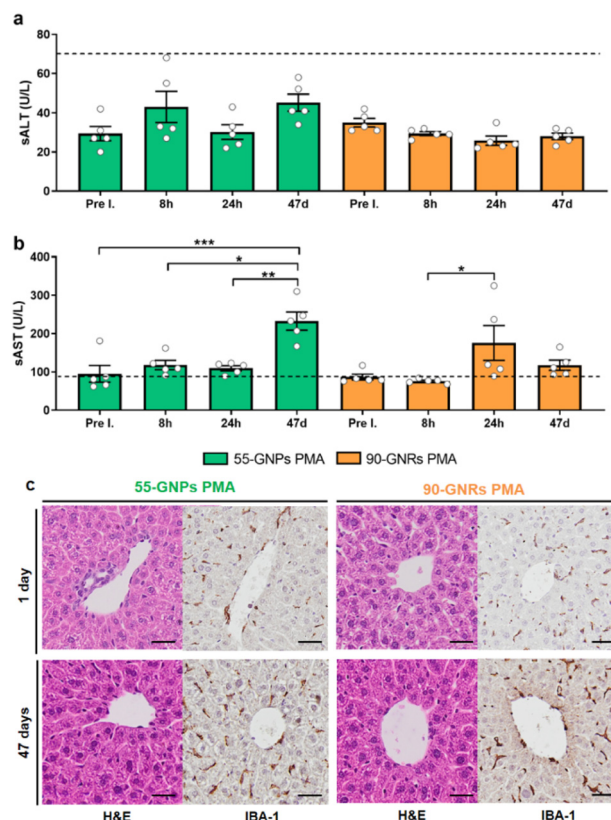


**Fig. 7** Hepatic transaminases levels in serum and liver histology by H&E and IBA-1 staining after NPs injection. (a and b) Activity (units liter<sup>-1</sup> [U L<sup>-1</sup>]) of serum (a) ALT and (b) AST measured at the indicated time points in groups of mice injected with PMA-coated NPs 55-GNPs and 90-GNRs with respect to the vehicle. Dashed lines indicated the upper value of normality of each variable (70 U L<sup>-1</sup> for ALT and 83 U L<sup>-1</sup> for AST). Data were presented as mean ± S.E.M. *P* values were determined by one-way ANOVA with Bonferroni's correction \**P* < 0.05, \*\**P* < 0.01 and \*\*\**P* < 0.001. (c) H&E and IBA-1 staining in livers treated with GNPs after 1 and 47 days. Scale bars = 50 μm.

transaminase (sAST), hepatic enzymes which activities are elevated during liver damage, were quantified to detect possible inflammation or necrosis in tissue. As it is shown in Fig. 7a (Fig. S12†), no value was over the maximum level of normality for sALT, 70 U L<sup>-1</sup> (dashed line), the most specific and sensitive biomarker for liver injury. A significant increase of sAST, was observed for spherical NPs after 47 days and after 24 hours for rod-like NPs, overpassing the maximum value of normality for sAST of 83 U per L per mice (Fig. 7b and Fig. S13†). However, the enzyme sAST is not specific for the liver, an increase in its levels could be due to damage to the liver, skeletal muscle or any other cell that suffers lysis such as red blood cells. Histological evaluation with H&E and IBA-1 staining in liver tissues after 24 hours and 47 days (Fig. 7c and Fig. S14–S17†) did not show any sign of inflammation, steatosis, fibrosis or hepatocyte necrosis in comparison with the control mice (Fig. S14–S16†). Also, macroscopic examination of all organs, weight loss, diarrhea, inability to walk or other types of clinical signs were not observed in mice, demonstrat-





ing that GNPs even if they accumulate in the liver, they did not cause any type of toxic effect over time.

## Conclusions

Overall, our data strongly suggest that the hepatic filtering of GNPs, after bloodstream circulation, may be influenced by their geometry and the polymer coating on their surface. However, these parameters almost exclusively influenced the kinetics of penetration in the liver that very often occurs in the first hours after administration for all types of GNPs. On the other hand, once penetrated in the liver, their fate seems independent of the physical–chemical nature of GNPs. By an integrated method of analysis combining ICP-MS, AMG, TEM and SIM, we were able to demonstrate that all type of GNPs remained entrapped in endothelial or, more frequently, macrophagic lysosomes not undergoing to an expected process of biodegradation or clearance by exocytosis of multivesicular bodies. A similar behaviour was also seen in terms of biocompatibility; it is indeed interesting to note that, despite the large presence of GNPs at least up until the 7th week after administration neither acute nor chronic markers of hepatic dysfunction were found. We can conclude here that independently of the NPs size, shape and surface chemistry for the set of NPs under study, spherical and nanorods with sizes between 25 and 90 nm, accumulated in the liver within 1 day and remained in Kupffer cells and LSECs for 47 days. The percentage of GNPs reaching the liver is strongly affected by their size and aspect ratio, being 20% of the given dose for the 25-GNPs and up to 70% for the nanorods. However, in all cases, what reaches the liver remains practically intact there. This is a fundamental finding with large implications for the use of GNPs for nanomedicine and the size and dose of GNPs must be carefully controlled to avoid long-term accumulation in the liver.

## Author contributions

J. F. A., M. S., P. B., M. M. conceived the idea and planned the experiments. J. F. A., M. S., T. U. L., E. C., M. B. V., M. D., F. F., A. C., C. C., G. S. conducted the experiments. J. F. A. and M. S. prepared the figures. J. F. A. and P. B. wrote the manuscript, and all others contributed to revisions.

## Conflicts of interest

There are no conflicts to declare.

## Acknowledgements

This project has received funding from the European Union's Horizon 2020 research and innovation program under the Marie Skłodowska-Curie grant agreement no. 814236 - Nanocarb. M. S. acknowledges the H2020-MSCA-IF grant no.

894656. G. S. is supported by the Italian Association for Cancer Research (AIRC) grants 22820 and 22737.

## References

- 1 M. J. Mitchell, M. M. Billingsley, R. M. Haley, M. E. Wechsler, N. A. Peppas and R. Langer, *Nat. Rev. Drug Discovery*, 2021, **20**, 101–124.
- 2 B. Li and L. A. Lane, *Wiley Interdiscip. Rev.: Nanomed. Nanobiotechnol.*, 2019, **11**, e1542.
- 3 M. G. Soliman, B. Pelaz, W. J. Parak and P. del Pino, *Chem. Mater.*, 2015, **27**, 990–997.
- 4 L. Talamini, M. B. Violatto, Q. Cai, M. P. Monopoli, K. Kantner, Ž. Krpetić, A. Perez-Potti, J. Cookman, D. Garry, C. P. Silveira, L. Boselli, B. Pelaz, T. Serchi, S. Cambier, A. C. Gutleb, N. Feliu, Y. Yan, M. Salmona, W. J. Parak, K. A. Dawson and P. Bigini, *ACS Nano*, 2017, **11**, 5519–5529.
- 5 W. G. Kreyling, A. M. Abdelmonem, Z. Ali, F. Alves, M. Geiser, N. Haberl, R. Hartmann, S. Hirn, D. J. de Aberasturi, K. Kantner, G. Khadem-Saba, J.-M. Montenegro, J. Rejman, T. Rojo, I. R. de Larramendi, R. Ufartes, A. Wenk and W. J. Parak, *Nat. Nanotechnol.*, 2015, **10**, 619–623.
- 6 K. Sztandera, M. Gorzkiewicz and B. Klajnert-Maculewicz, *Mol. Pharm.*, 2019, **16**, 1–23.
- 7 P. Picchetti, G. Moreno-Alcántar, L. Talamini, A. Mourgout, A. Aliprandi and L. De Cola, *J. Am. Chem. Soc.*, 2021, **143**, 7681–7687.
- 8 L. Talamini, P. Picchetti, L. M. Ferreira, G. Sitia, L. Russo, M. B. Violatto, L. Travaglini, J. Fernandez Alarcon, L. Righelli, P. Bigini and L. De Cola, *ACS Nano*, 2021, **15**, 9701–9716.
- 9 J. Kolosnjaj-Tabi, Y. Javed, L. Lartigue, J. Volatron, D. Elgrabli, I. Marangon, G. Pugliese, B. Caron, A. Figuerola, N. Luciani, T. Pellegrino, D. Alloyeau and F. Gazeau, *ACS Nano*, 2015, **9**, 7925–7939.
- 10 A.-L. Bailly, F. Correard, A. Popov, G. Tselikov, F. Chaspoul, R. Appay, A. Al-Kattan, A. V. Kabashin, D. Braguer and M.-A. Esteve, *Sci. Rep.*, 2019, **9**, 12890.
- 11 Y. Jiang, S. Huo, T. Mizuhara, R. Das, Y.-W. Lee, S. Hou, D. F. Moyano, B. Duncan, X.-J. Liang and V. M. Rotello, *ACS Nano*, 2015, **9**, 9986–9993.
- 12 P. Decuzzi and M. Ferrari, *Biomaterials*, 2007, **28**, 2915–2922.
- 13 M. P. Monopoli, C. Åberg, A. Salvati and K. A. Dawson, *Nat. Nanotechnol.*, 2012, **7**, 779–786.
- 14 A. E. Nel, L. Mädler, D. Velegol, T. Xia, E. M. V. Hoek, P. Somasundaran, F. Klaessig, V. Castranova and M. Thompson, *Nat. Mater.*, 2009, **8**, 543–557.
- 15 K. A. Dawson and Y. Yan, *Nat. Nanotechnol.*, 2021, **16**, 229–242.
- 16 A. Salvati, A. S. Pitek, M. P. Monopoli, K. Prapainop, F. B. Bombelli, D. R. Hristov, P. M. Kelly, C. Åberg, E. Mahon and K. A. Dawson, *Nat. Nanotechnol.*, 2013, **8**, 137–143.



- 17 E. Papini, R. Tavano and F. Mancin, *Front. Immunol.*, 2020, **11**, 567365.
- 18 K. K. Sørensen and B. Smedsrød, *The liver: biology and pathobiology*, John Wiley & Sons Ltd, New Jersey, 2020.
- 19 A. Balfourier, N. Luciani, G. Wang, G. Lelong, O. Ersen, A. Khelfa, D. Alloeyau, F. Gazeau and F. Carn, *Proc. Natl. Acad. Sci. U. S. A.*, 2020, **117**, 103–113.
- 20 P. Falagan-Lotsch, E. M. Grzincic and C. J. Murphy, *Proc. Natl. Acad. Sci. U. S. A.*, 2016, **113**, 13318–13323.
- 21 C. Hanske, G. González-Rubio, C. Hamon, P. Formentín, E. Modin, A. Chuvilin, A. Guerrero-Martínez, L. F. Marsal and L. M. Liz-Marzán, *J. Phys. Chem. C*, 2017, **121**, 10899–10906.
- 22 X. Ye, L. Jin, H. Caglayan, J. Chen, G. Xing, C. Zheng, V. Doan-Nguyen, Y. Kang, N. Engheta, C. R. Kagan and C. B. Murray, *ACS Nano*, 2012, **6**, 2804–2817.
- 23 M. Xu, M. G. Soliman, X. Sun, B. Pelaz, N. Feliu, W. J. Parak and S. Liu, *ACS Nano*, 2018, **12**, 10104–10113.
- 24 C.-A. J. Lin, R. A. Sperling, J. K. Li, T.-Y. Yang, P.-Y. Li, M. Zanella, W. H. Chang and W. J. Parak, *Small*, 2008, **4**, 334–341.
- 25 EuNCL Endotoxin Levels Online, [https://euncl.org/about-us/assay-cascade/PDFs/Prescreening/EUNCL-STE-001\\_2\\_2.pdf?m=1476164492](https://euncl.org/about-us/assay-cascade/PDFs/Prescreening/EUNCL-STE-001_2_2.pdf?m=1476164492), accessed January 2023.
- 26 N. C. Bell, C. Minelli and A. G. Shard, *Anal. Methods*, 2013, **5**, 4591.
- 27 K. A. Willets and R. P. Van Duyne, *Annu. Rev. Phys. Chem.*, 2007, **58**, 267–297.
- 28 W. Haiss, N. T. K. Thanh, J. Aveyard and D. G. Fernig, *Anal. Chem.*, 2007, **79**, 4215–4221.
- 29 N. G. Khlebtsov, *Anal. Chem.*, 2008, **80**, 6620–6625.
- 30 A. Konwar, D. Chowdhury and A. Dan, *Mater. Chem. Front.*, 2019, **3**, 716–725.
- 31 S. Klein, S. Petersen, U. Taylor, D. Rath and S. Barcikowski, *J. Biomed. Opt.*, 2010, **15**, 036015.
- 32 L. Guerrini, R. Alvarez-Puebla and N. Pazos-Perez, *Materials*, 2018, **11**, 1154.
- 33 L. Shi, J. Zhang, M. Zhao, S. Tang, X. Cheng, W. Zhang, W. Li, X. Liu, H. Peng and Q. Wang, *Nanoscale*, 2021, **13**, 10748–10764.
- 34 K. M. Tsoi, S. A. MacParland, X.-Z. Ma, V. N. Spetzler, J. Echeverri, B. Ouyang, S. M. Fadel, E. A. Sykes, N. Goldaracena, J. M. Kathis, J. B. Conneely, B. A. Alman, M. Selzner, M. A. Ostrowski, O. A. Adeyi, A. Zilman, I. D. McGilvray and W. C. W. Chan, *Nat. Mater.*, 2016, **15**, 1212–1221.
- 35 E. Clemente, M. Martinez-Moro, D. N. Trinh, M. G. Soliman, D. I. R. Spencer, R. A. Gardner, M. Kotsias, A. Sánchez Iglesias, S. Moya and M. P. Monopoli, *J. Colloid Interface Sci.*, 2022, **613**, 563–574.
- 36 D. N. Trinh, R. A. Gardner, A. N. Franciosi, C. McCarthy, M. P. Keane, M. G. Soliman, J. S. O'Donnell, P. Meleady, D. I. R. Spencer and M. P. Monopoli, *ACS Nano*, 2022, **16**, 5463–5475.
- 37 R. A. Petros and J. M. DeSimone, *Nat. Rev. Drug Discovery*, 2010, **9**, 615–627.
- 38 G. Sonavane, K. Tomoda and K. Makino, *Colloids Surf., B*, 2008, **66**, 274–280.
- 39 C. Ruggiero, L. Pastorino and O. L. Herrera, in 2010 Annual International Conference of the IEEE Engineering in Medicine and Biology, IEEE, Buenos Aires, 2010, pp. 3731–3732.
- 40 H. Gao, W. Shi and L. B. Freund, *Proc. Natl. Acad. Sci. U. S. A.*, 2005, **102**, 9469–9474.
- 41 M. R. K. Ali, M. A. Rahman, Y. Wu, T. Han, X. Peng, M. A. Mackey, D. Wang, H. J. Shin, Z. G. Chen, H. Xiao, R. Wu, Y. Tang, D. M. Shin and M. A. El-Sayed, *Proc. Natl. Acad. Sci. U. S. A.*, 2017, **114**, E3110–E3118.
- 42 P. Saftig and J. Klumperman, *Nat. Rev. Mol. Cell Biol.*, 2009, **10**, 623–635.
- 43 P. Lajoie, G. Guay, J. W. Dennis and I. R. Nabi, *J. Cell Sci.*, 2005, **118**, 1991–2003.
- 44 M. Borkowska, M. Siek, D. V. Kolygina, Y. I. Sobolev, S. Lach, S. Kumar, Y.-K. Cho, K. Kandere-Grzybowska and B. A. Grzybowski, *Nat. Nanotechnol.*, 2020, **15**, 331–341.
- 45 B. D. Chithrani, A. A. Ghazani and W. C. W. Chan, *Nano Lett.*, 2006, **6**, 662–668.
- 46 R. Augustine, A. Hasan, R. Primavera, R. J. Wilson, A. S. Thakor and B. D. Kevadiya, *Mater. Today Commun.*, 2020, **25**, 101692.

